Journal of Computational Physics **174,** 277–305 (2001)
doi:10.1006/jcph.2001.6906, available online at http://www.idealibrary.com on IDEAL®

On the Efficient Numerical Simulation of Directionally Spread Surface Water Waves

W. J. D. Bateman,* C. Swan,* and P. H. Taylor†

**Department of Civil & Environmental Engineering, Imperial College, SW7 2UB, London, United Kingdom; and †Department of Engineering Science, Oxford University, OX1 3PJ, Oxford, United Kingdom*
E-mail: w.bateman@ic.ac.uk; c.swan@ic.ac.uk; paul.taylor@eng.ox.ac.uk

Received February 2, 2001; revised August 3, 2001

This paper concerns the description of transient and highly nonlinear, near-breaking, surface water waves that are characterized by a spread of wave energy in both frequency and direction. A new spectral wave model is described that allows both the unsteadiness and the directionality of a wave field to be described in a fully nonlinear sense. The methodology underlying the scheme is similar to the unidirectional model developed previously by Craig and Sulem [13]. An approximation of the Dirichlet–Neumann operator is made that transforms the boundary values of the velocity potential, ϕ, at the water surface into values of ϕ_z. This allows an initial spatial representation of the water surface elevation and the velocity potential on this surface to be time marched using fast Fourier transforms. The advantages of this technique lie in both its efficiency and its robustness. These are of fundamental importance when seeking to model extreme ocean waves, involving broad-banded frequency spectra and realistic directional spreads, since they incorporate a large range of horizontal length scales. In its present form, the model is appropriate to waves propagating on water of constant depth; it runs on a PC and is sufficiently stable to predict the evolution of near-breaking waves. Indeed, the only significant restriction arises due to the Fourier series representation. This requires the water surface elevation to be a single-valued function of the horizontal coordinates and therefore limits the model to non-overturning waves. The new numerical scheme is validated against a fifth-order Stokes solution for regular waves and the recent experimental observations provided by Johannessen and Swan [3]. These latter comparisons are particularly important, confirming that the model is able to describe the rapid and highly significant energy transfers that occur across the wavenumber spectrum in the vicinity of an extreme event. These are strongly dependent upon the directionality of the wavefield and critically important when seeking to define the characteristics of an extreme, near-breaking, wave. The paper concludes with an example of the formation of a realistic, fully nonlinear and directionally spread wave group in the open ocean. © 2001 Elsevier Science

Key Words: directional water waves; extreme ocean waves; 3-D wave modelling; nonlinear wave–wave interactions; numerical wave modeling.

0021-9991/01 $35.00
© 2001 Elsevier Science
All rights reserved

1. INTRODUCTION

In an ocean environment a surface wavefield is characterized by a spread of energy in both frequency and direction. From an engineering perspective, design criteria are based upon extreme waves occurring in the most severe storms representing the 1 in 100 year or perhaps the 1 in 10,000 year event. Such waves are both strongly nonlinear and highly transient, where the former implies complex interaction between the energy modes and the latter ensures that the highest or steepest water surface elevations disperse rapidly in both space and time. Comparisons between field measurements (notably, Jonathan and Taylor [1]) and unidirectional "focused" wave groups generated in a laboratory wave flume (Baldock, *et al.* [2]) suggest that the directionality of a wavefield plays a critical role in determining the characteristics of an extreme wave event.

Direct evidence of the importance of directionality is provided by recent laboratory observations in which Johannessen and Swan [3] report the first detailed observations of "focused" wave groups involving wave components that are spread in both frequency and direction. Although both the frequency and the directional distributions are much simplified compared to those typically occurring in the open ocean, these measurements have established three important points:

(a) If, for a given underlying frequency distribution, the linear sum of the component wave amplitudes is held constant, an increase in the directional spread leads to reduced nonlinearity for an extreme event with lower crest-trough asymmetry and hence smaller maximum crest elevations.

(b) Conversely, if the amplitudes of the wave components (corresponding to a given normalized frequency spectrum) are increased until the onset of wave breaking, an increase in the directional spread allows larger maximum limiting crest elevations.

(c) In the vicinity of an extreme event, the local nonlinear interactions produce new and previously unexpected high-frequency components. These are quite distinct from the well-established frequency-sum terms arising at a second order of wave steepness (Longuet-Higgins and Stewart [4]). Furthermore, there is strong evidence to suggest that much of this high-frequency energy is freely propagating. This apparent broadening of the free-wave regime in the vicinity of an extreme is again dependant on the underlying directionality and plays an important role in defining the characteristics of the extreme water surface elevation.

Despite the practical importance of these issues, they cannot be modeled using existing wave solutions. At the simplest level, common design wave solutions either apply a linear random wave theory, which neglects the nonlinearity altogether, or a classical Stokes' expansion that includes nonlinearity but neglects the distribution of energy in the frequency domain. Directionality, if it is included at all, is usually approximated by an "in-line" velocity reduction factor, based on either simple linear arguments or a best fit to (limited) empirical data. At a higher level of sophistication, a first approximation to the bound wave structure may be described by a Stokes-type perturbation expansion to second-order in terms of the interaction of linear components (Longuet-Higgins and Stewart [4] and Sharma and Dean [5]). Although such solutions are of undoubted value, identifying both the frequency-sum and the frequency-difference terms, it is well known that such low-order expansions are restricted to wave systems of moderate steepness.

Above this level of approximation, linear dispersion is no longer applicable and a theoretical model must allow for resonant wave–wave interactions. This accounts for the flow of energy between different but related wave components. Such solutions may be based upon the mode-coupling models originating from the experimental observations and theory of Benjamin and Feir [6] or may involve solutions to the nonlinear evolution equations (NLEEs), such as the extended Schrödinger equation of Lo and Mei [7]. Formulations based on either of these approaches are usually solved numerically using pseudo-spectral schemes involving fast Fourier transforms at successive time steps. Although such solutions are efficient, with computational effort scaling as $\hat{N}\,log(\hat{N})$ (where $\hat{N}$ is the number of components included), they cannot be applied to waves that are very steep or to those that involve a large range of length scales. This latter constraint is particularly restrictive in the context of ocean waves for which the frequency spectra are typically broadbanded.

Having discounted both the mode-coupling models and solutions of the NLEEs, the next level of sophistication involves the numerical solution of the exact (Euler) equations of motion for water waves. Longuet-Higgins and Cokelet [8] first outlined the calculation procedure whereby a wavefield, initially specified in the spatial domain, could be time marched using the nonlinear free surface boundary conditions (Section 2 below). Although several alternative formulations for unidirectional waves now exist, only one pseudo-spectral approach has been extended in a fully nonlinear sense to include directionality. Johannessen and Swan [9] have applied the Fourier-based scheme proposed by Fenton and Rienecker [10] to model multidirectional wave groups in water of constant depth. Although this model is successful when compared to narrow-banded laboratory data, it is relatively inefficient, with computational effort rising in proportion to $\hat{N}^3$. This limits its ability to model realistic broadbanded ocean spectra.

In a unidirectional context, more efficient boundary integral models exist, with run times proportional to $\hat{N}^2$. In particular, Dold and Peregrine [11] outline a scheme, based on the Cauchy integral formula, that is highly accurate, stable, and computationally efficient. Unfortunately, such schemes cannot easily be extended to include a third dimension. Other methods based around the Green function can be adapted to include a third dimension, as demonstrated by Isaacson and Cheung [12]. However, this model only satisfied a second-order approximation of the governing equations. Attempts to satisfy the fully nonlinear equations have resulted in very unstable solutions. Accordingly, even the most sophisticated wave models are unable to provide a physically realistic description of extreme ocean waves.

The present paper addresses this point. It provides a new, fully nonlinear wave model appropriate to the description of extreme waves arising in realistic ocean spectra, characterized by a significant spread of energy in both frequency and direction. Section 2 commences with a brief review of the governing equations and their application in a time-marching solution. A major improvement to the Fourier-based scheme for unidirectional waves (Craig and Sulem [13]) is also introduced. This involves the introduction of the Dirichlet–Neumann operator, referred to as the G-operator, to transform values of the velocity potential on the water surface into the vertical derivative of the velocity potential. As a consequence, run times proportional to $\hat{N}\,log(\hat{N})$ are achieved. Although this solution is in some respects less capable than the Cauchy integral formulations (with the surface restricted to a single-value function of the spatial position, solutions cannot be advanced beyond the point of wave overturning), it has the overriding advantage of being expandable to three

dimensions. Section 2 concludes with a brief outline of the proposed 3-D solution. The derivation of the new 3-D G-operator is given in Section 3, while Section 4 describes the numerical formulation including the time-marching procedure, the need for filtering and the numerical accuracy. The initial conditions appropriate to the commencement of the scheme are discussed in Section 5, and some preliminary results are provided to demonstrate the success of the proposed model. In Section 6 comparisons are first provided with laboratory data [3] involving highly nonlinear, near-breaking wave groups that are spread in both frequency and direction. Several test cases are considered and the numerical predictions shown to be in very good agreement with the observed data. In the second part of this section, full-scale calculations are undertaken involving an extreme wave in a JONSWAP spectrum. This corresponds to a typical 1 in 100 year design event (for the northern North Sea) and represents the first calculations, involving a realistic broadbanded spectrum, that are both fully nonlinear and directionally spread. Concluding remarks and suggestions for further work are given in Section 7.

2. BACKGROUND

2.1. Governing Equations

The required solution must satisfy the governing equations for the evolution of a wavefield propagating on the free surface of a three-dimensional body of fluid. If the wave-induced fluid motion is assumed irrotational, a velocity potential $\phi(x, y, z, t)$ can be defined where t indicates time and (x, y, z) represent the usual Cartesian coordinates in which (x, y) defines a horizontal plane located at the mean water level and z is measured vertically upward. The velocity vector, $\mathbf{u} = (u, v, w)$, is defined by $\mathbf{u} = \nabla\phi$, where $\nabla = (\partial_x, \partial_y, \partial_z)$. If the fluid is assumed to be incompressible, mass continuity requires $\nabla\mathbf{u} = 0$, which, expressed in terms of ϕ yields Laplace's equation, is

$$\nabla^2\phi = 0 \tag{1}$$

This equation applies throughout the fluid domain, $\mathfrak{D}_\eta$, which is bounded by a horizontal bed at $z = -h$ and the free surface defined by $z = \eta(x, y, t)$. On these boundaries the conditions apply:

$$\phi_z = 0 \quad \text{on} \quad z = -h \tag{2}$$

and

$$\left.\begin{aligned} \phi_t + \tfrac{1}{2}|\nabla\phi|^2 + g\eta &= 0 \\ \eta_t + \eta_x\phi_x + \eta_y\phi_y - \phi_z &= 0 \end{aligned}\right\} \quad \text{on} \quad z = \eta(x, y, t), \tag{3a \& 3b}$$

where g is the gravitational acceleration and the subscript denotes differentiation with respect to the variable. The first of these equations (2) denotes the fact that the horizontal bed is assumed impermeable, while the latter (3a) and (3b) define the dynamic and kinematic free surface boundary conditions. These conditions respectively require the pressure at the water surface to be constant and the fluid particles on the surface to remain there.

Equations (3a) and (3b) provide the basis of all time-marching solutions. Simple rearrangement defines ϕ_t and η_t in terms of η and the spatial derivatives of η and ϕ evaluated

at the water surface. If at some initial time, $t = t_0$, a spatial representation of η and ϕ is given, and it is assumed that their gradients in the x, y, and z directions can be evaluated, η_t and ϕ_t can be defined and the solution successfully time marched to $t = t_0 + \Delta t$. With an appropriate concern for accuracy, repeated application allows the evolution of the wavefield over large times.

2.2. Application of the Dirichlet–Neumann Operator

In unidirectional waves, the early Fourier-based spectral method of Fenton and Rienecker [10] described the surface elevation

$$\eta(x) = \sum_{n=0}^{N/2} a_n e^{ik_n x} \tag{4}$$

and the corresponding velocity potential

$$\phi(x, z) = \sum_{n=0}^{N/2} A_n \cosh(k_n(z + h)) e^{ik_n x}, \tag{5}$$

where a_n and A_n are functions of time only, $k_n = nk_0$ is an integer multiple of the fundamental wavenumber $k_0 = 2\pi/\lambda_0$ (where λ_0 is the fundamental wave length), $N/2$ represents the number of terms in the Fourier series, and N is number of surface calculation points. In this form, the water surface elevation (4) can be represented by a Fourier series, while the explicit inclusion of z in the velocity potential (5) avoids the difficulty of defining the spatial gradient ϕ_z at the water surface (Eqs. (3a) and (3b)). Unfortunately, the downside of this approach is that while the surface elevation can be time stepped using a fast Fourier transform (FFT), the derivatives $(A_n)_t$ needed to advance ϕ require the solution of a matrix of N simultaneous equations. This latter activity is responsible for the scheme's poor computational efficiency and severe limitations when extended to three dimensions.

Using a theorem proposed by Coifman and Meyer [14], Craig and Sulem [13] introduced a Dirichlet–Neumann operator, referred to as their G-operator, to convert values of the velocity potential on the water surface, $\phi(x, (\eta(x, t), t) = \Phi(x, t)$, into its spatial derivatives. In a formal sense, the Dirichlet–Neumann operator concerns the normal derivative $\partial_n \phi$, where n is an outward facing normal. However, Craig and Sulem [13] defined their G-operator such that

$$G(\eta)\Phi = (\phi_z - \eta_x \phi_x)_{z=\eta}. \tag{6}$$

In this way, the kinematic free surface boundary condition (3b) appropriate to unidirectional waves ($\eta_y = \phi_y = 0$) becomes

$$\eta_t = G(\eta)\Phi. \tag{7a}$$

Noting that the temporal derivative of the surface velocity potential is defined by $\Phi_t = (\phi_t + \phi_z \eta_t)_{z=\eta}$, where the second term in the brackets reflects the vertical motion of the surface profile, the dynamic free-surface boundary condition (Eq. (3a)) is rearranged to

give

$$\Phi_t = -\frac{1}{2(1+(\eta_x)^2)}((\Phi_x)^2 - (\eta_t)^2 - 2\,\eta_x \Phi_x \eta_t) - g\eta. \tag{7b}$$

Using Eqs. (7a) and (7b) the surface parameters η and Φ can be time stepped in the usual way. The advantage of this approach is that for unidirectional waves, only equations involving terms on the one-dimensional free surface need to be solved, with both η and Φ represented by a Fourier series. It is this approach that the present paper seeks to extend to multidirectional wavefields.

More recently, Craig *et al.* [15] and Nicholls [16] have provided descriptions of the Dirichlet–Neumann operator for three-dimensional domains. In the latter case, Nicholls [16] applied numerical continuation methods to both two- and three-dimensional wave problems. However, the computational efficiency of this scheme is such that parallel computating power is required to resolve a small number of wave components. In contrast, the present paper adopts an alternative formulation, based on the scheme originally outlined by Craig and Sulem [13], and seeks to model a large number of interacting wave components typical of those occurring in a real sea state.

2.3. Solution Procedure

Before providing a full derivation of the new three-dimensional G-operator, it is of value to give a brief overview of the solution procedure. If the dependant variables ϕ and η are to be represented by Fourier series in the horizontal plane, one possible solution assumes that the wave motion is periodic in both the x and y directions. If λ_x and λ_y define the fundamental wavelengths in the x and y directions, $\eta(x+\lambda_x, y+\lambda_y) = \eta(x,y)$ and $\phi(x+\lambda_x, y+\lambda_y, z) = \phi(x,y,z)$, defining a fundamental domain that is rectangular in character. At this point, it is perhaps of interest to note that there are other periodic domains for functions of two variables that are not necessarily rectangular. These nonrectangular domains are not considered in the present paper, but may be important when considering some doubly periodic motions such as the five-wave reasonant interactions that occur in deep water.

In the present rectangular domain, one class of solution that satisfies the periodic constraint noted above is given by

$$\phi = \sum_{k=-\infty}^{\infty} \sum_{l=-\infty}^{\infty} a_{kl}(z) e^{i(kx+ly)}. \tag{8}$$

In a Fourier system, k and l are integer multiples of the fundamental wavenumber components in the x and y directions, respectively, so that $k = k_0 n$ and $l = l_0 m$, where $k_0 = 2\pi/\lambda_x$, $l_0 = 2\pi/\lambda_y$, and n and m are integers. The unknown local constants $a_{kl}(z)$ may be defined in terms of global parameters by substituting Eq. (8) into (1) and solving the resulting partial differential equation subject to the boundary conditions given in Eq. (2). This yields

$$\phi = \sum_{k=-\infty}^{\infty} \sum_{l=-\infty}^{\infty} \alpha_{kl}\, \cosh(K(z+h)) e^{i(kx+ly)}, \tag{9a}$$

where $K = \sqrt{k^2+l^2}$ and the parameters α_{kl} are global constants. Evaluating ϕ at the water

surface, $z = \eta$, gives

$$\Phi = \sum_{k=-\infty}^{\infty} \sum_{l=-\infty}^{\infty} \alpha_{kl} \cosh(K(\eta + h)) e^{i(kx+ly)}. \tag{9b}$$

The solution procedure now requires a new three-dimensional G-operator that transforms Φ into ϕ_z evaluated at $z = \eta$:

$$(\phi_z)_{z=\eta} = G(\eta)\Phi. \tag{10}$$

Using Eq. (9a),

$$(\phi_z)_{z=\eta} = \sum_{k=-\infty}^{\infty} \sum_{l=-\infty}^{\infty} \alpha_{kl} K \sinh(K(\eta + h)) e^{i(kx+ly)}. \tag{11}$$

Comparing Eqs. (9b), (10), and (11) the transformation implied by the G-operator simply involves the "multiplication" by $K \tanh(K(\eta + h))$ for all values of k, l, x, and y. Unfortunately, multiplications in x, y space and Fourier multiplications in k, l space do not commute, a fact that is closely related to the Heisenburg uncertainty principle [17]. This is a particular problem in the evaluation of $\tanh(K(\eta + h))$, which contains information in both the wavenumber domain and the physical domain.

To overcome this difficulty, the cosh and sinh terms in Eqs. (9b) and (11) are expanded using a Taylor series expansion about $\eta = 0$. In these expansions, "multiplications" appropriate to the two domains can be resolved, with Fourier transforms (FTs) used to convert between the wavenumber and physical domains. Substituting these expansions into Eq. (10) allows the G-operator to be evaluated at various orders. In this way, a solution appropriate for all k, l, x, and y is achieved.

Having evaluated the new 3-D G-operator (10), the partial derivatives of ϕ evaluated at $z = \eta$ may be defined in a similar manner to that outlined in Section 2.2 giving:

$$(\phi_x)_{z=\eta} = \Phi_x - \eta_x G(\eta)\Phi \tag{12a}$$

$$(\phi_y)_{z=\eta} = \Phi_y - \eta_y G(\eta)\Phi \tag{12b}$$

$$(\phi_t)_{z=\eta} = \Phi_t - \eta_t G(\eta)\Phi. \tag{12c}$$

Applying these results the two nonlinear boundary conditions can be rewritten as

$$\eta_t = G(\eta)\Phi - (\eta_x \phi_x - \eta_y \phi_y)_{z=\eta} \tag{13a}$$

$$\Phi_t = \eta_t G(\eta)\Phi - \frac{1}{2}(G(\eta)\Phi)^2 - \frac{1}{2}[(\phi_x)^2 + (\phi_y)^2]_{z=\eta} - g\eta \tag{13b}$$

It is these equations that will be time marched to define the evolution of a fully nonlinear and directionally spread wavefield.

3. THE NEW 3-D G-OPERATOR

3.1. Mathematical Derivation

Coifman and Meyer [14] illustrated that an operator of the form of $G(\eta)$ remains analytic provided the Lipschitz norm (the maximum slope) of η remains bounded by R, where

R is the radius of convergence. As the spectral (wavenumber) bandwidth of the problem increases R reduces, but $G(\eta)$ remains analytic provided the water surface (η) is neither locally very steep nor excessively far from the mean water level.

An analytic operator can be expanded in terms of a convergent Taylor expansion

$$G(\eta) = \sum_{j=0}^{\infty} G_j(\eta), \tag{14}$$

in which each $G_j(\eta)$ is homogeneous and of degree j in η such that

$$G_j(\beta\eta) = \beta^j G_j(\eta), \tag{15}$$

where β is a simple scaling parameter.

To obtain the homogeneous expansion of this operator, Eqs. (9b) and (11) are expanded about $\eta = 0$ using a Taylor series. Within these series expansions, successive derivatives are collected in terms of odd and even powers that conveniently segregate into $\cosh(kh)$ and $\sinh(kh)$. For simplicity these equations and those shown hereafter (until indicated otherwise) are for a single wavenumber component involving only one value of l and k. However, throughout the derivation it should be remembered that the overall solution must incorporate many wavenumber components. Expanding Eq. (9b) and (11) yields

$$\Phi = \left[\sum_{\substack{j>0 \\ j\text{even}}} \frac{1}{j!}(K\eta)^j \cosh(Kh) + \sum_{\substack{j>0 \\ j\text{odd}}} \frac{1}{j!}(K\eta)^j \sinh(Kh) \right] \alpha_{kl} e^{i(kx+ly)} \tag{16a}$$

$$(\phi_z)_{z=\eta} = \left[\sum_{\substack{j\geq 0 \\ j\text{even}}} \frac{K}{j!}(K\eta)^j \sinh(Kh) + \sum_{\substack{j>0 \\ j\text{odd}}} \frac{K}{j!}(K\eta)^j \cosh(Kh) \right] \alpha_{kl} e^{i(kx+ly)}. \tag{16b}$$

Substituting these expansions into Eq. (10) and dividing by $\cosh(Kh)$ gives

$$\left[\sum_{m=0}^{\infty} G_m(\eta) \right] \left[\sum_{\substack{j\geq 0 \\ j\text{even}}} \frac{1}{j!}(K\eta)^j + \sum_{\substack{j>0 \\ j\text{odd}}} \frac{1}{j!}(K\eta)^j \tanh(Kh) \right] \alpha_{kl} e^{i(kx+ly)}$$

$$= \left[\sum_{\substack{j\geq 0 \\ j\text{even}}} \frac{K}{j!}(K\eta)^j \tanh(Kh) + \sum_{\substack{j>0 \\ j\text{odd}}} \frac{K}{j!}(K\eta)^j \right] \alpha_{kl} e^{i(kx+ly)}. \tag{17}$$

To simplify this equation the summations on the left-hand side are reordered using the series law

$$\sum_{m=0}^{\infty} a_m \sum_{j=0}^{\infty} b_j = \sum_{j=0}^{\infty} \left(\sum_{m=0}^{j} a_m b_{j-m} \right) \tag{18}$$

to produce a summation of homogeneous powers from which even and odd terms of the same degree can be identified. Therefore, recursive formulas for all $G_j(\eta)\alpha_{kl}e^{i(kx+ly)}$ are obtained as follows.

For $j \geq 0$ and even

$$G_j(\eta)\alpha_{kl}e^{i(kx+ly)} = \frac{1}{j!}(\eta K)^j K \tanh(Kh)\alpha_{kl}e^{i(kx+ly)} - \sum_{\substack{m<j \\ m\text{even}}} G_m(\eta)\frac{1}{(j-m)!}(\eta K)^{j-m}\alpha_{kl}e^{i(kx+ly)} - \sum_{\substack{m<j \\ m\text{odd}}} G_m(\eta)\frac{1}{(j-m)!}(\eta K)^{j-m}\tanh(Kh)\alpha_{kl}e^{i(kx+ly)} \quad (19a)$$

For $j \geq 1$ and odd

$$G_j(\eta)\alpha_{kl}e^{i(kx+ly)} = \frac{1}{j!}(\eta K)^j K\alpha_{kl}e^{i(kx+ly)} - \sum_{\substack{m<j \\ m\text{odd}}} G_m(\eta)\frac{1}{(j-m)!}(\eta K)^{j-m}\alpha_{kl}e^{i(kx+ly)} - \sum_{\substack{m<j \\ m\text{even}}} G_m(\eta)\frac{1}{(j-m)!}(\eta K)^{j-m}\tanh(Kh)\alpha_{kl}e^{i(kx+ly)}. \quad (19b)$$

Equations (19a) and (19b) describe the solution for a single Fourier component. Using Fourier analysis, it may be shown that a solution appropriate to multiple components can be obtained by integrating over all wavenumber components,

$$f(D)\Phi(x,y) = \frac{1}{4\pi^2}\int\int f(K)\alpha_{kl}e^{i(kx+ly)}\,dk\,dl, \quad (20)$$

with

$$D = -i\,\partial_r \quad \text{and} \quad \alpha_{kl} = \int\int \Phi(x,y)e^{-i(kx+ly)}\,dx\,dy,$$

where D is a complex radial derivative operator in physical space, $r = \sqrt{x^2+y^2}$, and a_{kl} are the global constants found from a Fourier transform of Φ.

When $f(K) = 1$, Eq. (20) is simply the inverse Fourier transform, recreating the surface values of ϕ from the global constants α_{kl}. When Eq. (20) is applied to more complex functions, the results are of greater significance. For example, if $f(K) = K$, then Eq. (20) gives

$$\frac{1}{4\pi^2}\int\int K\alpha_{kl}e^{i(kx-ly)}\,dk\,dl = D\Phi, \tag{21a}$$

while if $f(K) = \tanh(K)$

$$\frac{1}{4\pi^2}\int\int \tanh(K)\alpha_{kl}e^{i(kx-ly)}\,dk\,dl = \tanh(D)\Phi. \tag{21b}$$

Applying this solution to all parts of Eqs. (19a) and (19b) transforms each $f(K)\alpha_{kl}e^{i(kx-ly)}$ term into $f(D)\Phi$. Accordingly, the first term of the G-operator ($j = 0$ in Eq. (19a)) is given by $G_0 e^{i(kx+ly)} = k\tanh(kh)\,\alpha_{kl}e^{i(kx+ly)}$, which becomes

$$G_0 = D\tanh(Dh). \tag{22a}$$

Similarly, the second and third terms are given by

$$G_1(\eta) = \eta D^2 - D\tanh(Dh)\eta D\tanh(Dh) \tag{22b}$$

$$G_2(\eta) = \frac{1}{2}\eta^2 D^2 D\tanh(Dh) - \eta D^2\eta D\tanh(Dh) - \frac{1}{2}D\tanh(Dh)\eta^2 D^2 + D\tanh(Dh)\eta D\tanh(Dh)\eta D\tanh(Dh). \tag{22c}$$

Although the calculation of these expressions is relatively easy, the number of FTs required for their evaluation increases rapidly with each additional order of the operator. Each time the D-operator (Eq. (20)) is encountered, two FTs are required. The first converts physical values to the wavenumber domain, where differentiation takes place, while the second transforms the values back into the physical domain. Accordingly, if M defines the order of truncation of Eq. (14), a total of $(2^{M+2} - 2)$ FTs are made with this recursive form.

To reduce the computational effort, Vijfvinkel [18] pioneered a method based on the elimination of repeated calculations and so speeded up the calculation of the original (2-D) G-operator [13]. Within the new 3-D G-operator, a separate study of the terms arising at each order has revealed a similar pattern of duplication. For example, the zero- and first-order terms both calculate $D\tanh(Dh)$. Therefore, the first-order term can be evaluated more efficiently using the result from G_0, such that $G_1(\eta) = \eta D^2 - D\tanh(Dh)\eta G_0$. This simple procedure reduces the FTs by two. Other more complex patterns also exist, speeding up the evaluation at each additional order. The "improved" method for evaluating Eqs. (22a)–(22c), together with the higher orders, may be summarized accordingly as

$$G_m(\eta)\Phi = \sum_{\substack{n\le m\\ n\text{odd}}} \frac{\eta^n D^{n+1}[\mu_{m-n}]}{n!} + \sum_{\substack{n\le m\\ n\text{even}}} \frac{\eta^n D^{n+1}\tanh(Dh)[\mu_{m-n}]}{n!}, \tag{23}$$

TABLE I
Number of FFTs Required to Evalutate the New G-operator

M	0	1	2	3	4	5	6	7	8	9
Original	2	6	14	30	62	126	254	510	1022	2046
Quick form	2	5	9	14	20	27	35	44	54	65

where

$$\mu_0 = \Phi$$

$$\mu_{j>0} = -\sum_{\substack{1\le n\le j \\ n\text{even}}} \frac{\eta^n D^n[\mu_{j-n}]}{n!} - \sum_{\substack{1\le n\le j \\ n\text{odd}}} \frac{\eta^n D^n \tanh(Dh)[\mu_{j-n}]}{n!}$$

Within this improved solution, the number of FTs is reduced to $\frac{1}{2}(M+1)(M+4)$. Since the overall computational effort is largely dependent upon the number of FTs calculated, the improvement associated with this latter scheme is significant, as indicated in Table I. For example, the numerical results presented in Section 6 were mostly undertaken with a truncation order of $M = 7$. In this case, the improved form of the equations is over an order of magnitude faster than the original, with no corresponding loss of accuracy.

3.2. Truncation Order

The optimal value for the truncation order M in Eq. (14) depends upon both the nonlinearity of the wave problem and the number of points (or Fourier components) used to define the water surface. To examine the characteristics of the operator, an analytical fifth-order unidirectional Stokes' solution [19] was used to calculate η and Φ, together with the corresponding vertical velocities arising at the water surface, for a unidirectional regular wave of period $T = 2.2$ s propagating in a water depth of $h = 1.2$ m. An equivalent set of vertical velocities arising at the water surface may also be calculated via the G-operator (in its 2-D form appropriate to unidirectional waves) based on the predicted values of η and Φ. Comparison between these velocities and the Stokes' results, where the latter are exact to fifth-order and consistent with η and Φ, highlights errors within the G-operator.

Figure 1 concerns the percentage errors in the surface velocities for a wide variety of test conditions. In both parts of this figure the dotted vertical line defines the truncation order ($M = 7$) adopted in the subsequent sections. These results demonstrate three important points in relation to the accuracy of the operator:

(a) When M is small, high-order corrections are negligible. In contrast, when M is large, numerical errors can quickly overwhelm any anticipated improvement from the highest-order contributions. This effect is apparent in both part (a) and (b) of Fig. 1, where there is a reduction in the errors up to some optimal truncation order. Beyond this point, the errors rapidly increase.

(b) Fig. 1a shows that as the number of surface points, N, increases up to 512, the optimal value of M also increases, resulting in smaller errors. An increase in N improves the description of the surface profile, which in turn allows η_x and Φ_x to be calculated

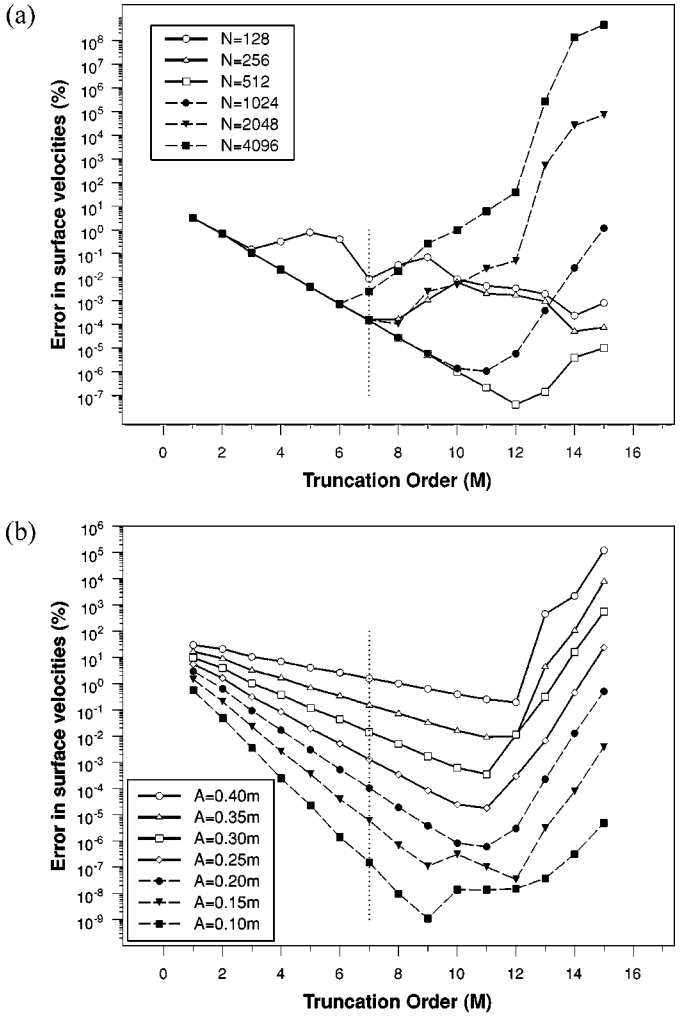

FIG. 1. Changes to the errors made within the G-operator. (a) As the number of surface points (N) is varied. $ka = 0.20$, $kh = 1.2$. (b) As the fundamental wave amplitude (A) is varied. $N = 1024$, $k = 0.96$ radm^{-1}, $h = 1.2$ m.

more accurately. However, for $N > 512$, the numerical errors become significant, reducing the optimal value of M. This is due to the wave energy being more finely spread across many wavenumber components, with each value becoming closer to the limits of the computers numerical accuracy (15 significant figures). This represents a significant restriction with all Fourier type models as it limits the range of wavelengths that can be modeled simultaneously.

(c) As the water surface becomes more nonlinear, the rate of improvement due to each additional order of the G-operator decreases, although the optimal truncation order increases (Fig. 1b). This reflects a balance between gaining accuracy from the evaluation of higher order terms and losing accuracy to numerical errors. Reducing the truncation order when modeling linear or near-linear waves is therefore beneficial, while an increase in the truncation order is appropriate as the waves become more nonlinear.

4. NUMERICAL FORMULATION

4.1. Implementation

The calculation of the G-operator and the remaining terms in Eqs. (13a) and (13b) requires the horizontal derivatives of Φ and η. The partial derivatives of each variable in the horizontal direction are achieved using FTs: a transformation into spectral space, followed by a multiplication by ik_n (for the calculation of ∂_x) and finally an inverse FT. These FTs are performed using a fast Fourier transform (FFT) technique, the characteristics of which are such that the number of calculations varies according to $N\ log(N)$, provided the number of surface points is an integer power of 2. Although there are numerous implementations of such schemes, each boasting superior performance in a variety of tasks, the current scheme is based upon the implementation developed by Frigo and Johnson [20] and known as the "fastest Fourier transform in the West" or FFTW. Using FFTW a large numerical run with $N = 256 \times 256$ surface points spends 60% of the computational time performing FFTs. In such a run, 20 wave periods involving a near-breaking wave event takes approximately 4 hours on a Pentium III 800 MHz computer.

4.2. Time Marching

Having identified the G-operator and the total horizontal derivatives of η and Φ at some initial time $t = t_0$, Eqs. (13a) and (13b) may be time marched to yield a description of the wavefield at some new time, $t = t_0 + \Delta t$, where Δt defines the time step. Within the present 3-D model, the time marching is achieved using a scheme similar to the fourth-order Adams–Bashford/Moulton predictor–corrector method outlined in Press *et al*. [21]. The only difference is that a fifth-order solution to Moulton's corrector is used, rather than the original fourth-order solution. Accordingly, the predictor is defined as

$$y_{n+1} = y_n + \frac{\Delta t}{24}\,(55\dot{y}_n - 59\dot{y}_{n-1} + 37\dot{y}_{n-2} - 9\dot{y}_{n-3}) + O(\Delta t^5) \tag{24a}$$

and the corrector as

$$y_{n+1} = y_n + \frac{\Delta t}{720}\,(251\dot{y}_{n+1} + 646\dot{y}_n - 264\dot{y}_{n-1} + 106\dot{y}_{n-2} - 19\dot{y}_{n-3}) + O(\Delta t^5), \tag{24b}$$

where the overdot denotes a derivative with respect to time. The adjustment to the corrector involves the inclusion of the term $\dot{y}_{n-3}$. Since this is already required in the predictor, the additional effort of including it is insignificant compared to the improvement in accuracy. To commence this scheme, the information required at the first three time steps is provided by a fourth-order Runge–Kutta method.

4.3. Filtering

In any time-marching scheme, the main source of numerical errors arises at those locations on the water surface where the rates of change of η are largest. This is primarily due to the difficulty of maintaining a sufficient degree of numerical accuracy when combining numbers of opposing size (i.e., $1 \times 10^3 + 1 \times 10^{-6}$). In addition, aliasing can also contribute to growth of high wavenumber errors, particularly when the energy is constrained within a small wavenumber range. After a large number of time steps, these difficulties can lead to spurious high-wavenumber oscillations in the water surface. Similar effects were observed

in the unidirectional models proposed by Dommermuth and Yue [22], Craig and Sulem [13], and Johannessen [24]. To overcome this difficulty, [22] proposed a five-point smoothing function to restrict the growth of unrealistically high wavenumbers, while [24] applied a simple cutoff filter.

The five-point filtering method was adapted for the present 3-D model by filtering radially away from the fundamental wavenumbers (k_0, l_0). The resulting filter function, $\Lambda(\hat{K}, \Psi)$, is described by

$$\Lambda(\hat{K}, \Psi) = \begin{cases} 1, & \hat{K} < \Psi \\ \frac{1}{8}[5 + 4\cos(\pi\hat{K}) - \cos(2\pi\hat{K}), & \Psi \le \hat{K} \le 1, \\ 0, & \hat{K} > 1 \end{cases}$$
$$\text{with the ratio } \hat{K} = \sqrt{\left(\frac{k}{k_{\max}}\right)^2 + \left(\frac{l}{l_{\max}}\right)^2}, \tag{25}$$

where $k_{\max}$ and $l_{\max}$ are the largest wavenumber values in each respective direction (x and y) and Ψ is a constant between 0 and 1 defining the level of filtering, $\Psi = 0$ representing the strongest filtering. Within the present study, $\Psi = 0.9$ was typically applied, although the exact value depends upon the spectral bandwidth of the problem under consideration. Indeed, the stability of the new numerical model was found to be such that in many cases no filtering at all was required. In the small number of cases where it was found to be necessary, it merely involved the suppression of very low energy levels located in the high-frequency tail of the spectrum. By using this approach we ensured that any difficulties associated with numerical accuracy and/or aliasing were rapidly overcome.

4.4. Accuracy

To monitor the accuracy of the numerical scheme, the total wave energy within the computational domain, E_{total}, was calculated at each time step using the solution proposed by Benjamin and Olver [23],

$$E_{\text{total}} = \frac{1}{2}\int_S (\Phi\eta_t + g\eta^2), \tag{26}$$

where the integration is performed over the entire water surface. Although Eq. (26) is exact, it only involves amplitude squared terms and is therefore only weakly weighted to those areas where the wave motion is most vigorous. Accordingly, very gradual shifts of energy throughout the domain may dwarf relatively large but strongly localized errors in the vicinity of an extreme or focused wave event. This difficulty becomes more significant as the size of the numerical domain increases relative to the wavelength corresponding to the peak of the spectrum.

In an attempt to overcome this concern, the reversibility of the solution was also considered. This involved undertaking a complete numerical run using the final results as the input to a second run in which the waves propagate backward. The ability of the scheme to reproduce the initial starting condition provides strong evidence that the errors associated with both the time-marching procedure (Eqs. (24a) and (24b)) and the numerical rounding are very small. Calculations of this type do not, however, provide guidance

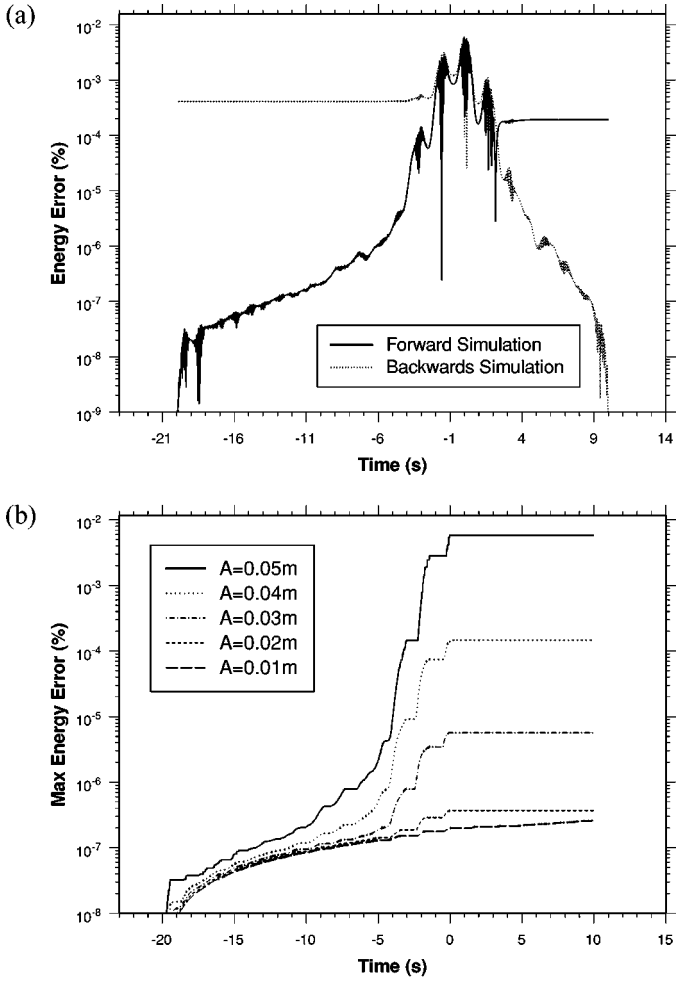

FIG. 2. Errors in the total energy for a laboratory-scale broadbanded sea state. (a) A comparison between forward and backward simulations for a near-breaking wave: $A = 55$ mm, $N = 512$, $\lambda_0 = 30$ m. (b) A comparison between runs with increasing nonlinearity: $N = 512$, $\lambda_0 = 30$ m.

as to the accuracy of either the G-operator or the FTs. These must be examined using Eq. (26).

Figures 2a and 2b provide a typical sequence of results, highlighting the accuracy of the proposed scheme. Figure 2a concerns a laboratory-scale sea state that evolves or focuses to produce a highly nonlinear, near-breaking, wave event at $t = 0$. Two error traces are presented. The first represents an initial run that commences at $t = -20$ s and continues through focus until $t = +10$ s. The second represents a reverse simulation in which the conditions at $t = +10$ s are run backward until $t = -20$ s. Comparing these results, the predicted water surface elevations are effectively identical, with a difference of only 2×10^{-6} m in the maximum crest elevation. Furthermore, the errors in total energy, Eq. (26), are also similar in the vicinity of the focused event with maximum errors in the forward run of 0.0058% compared to 0.0061% in the reverse run. Figure 2b again concerns a laboratory-scale sea state and contrasts the growth in the maximum error for five increasingly nonlinear wave groups, where A represents the linear sum of the component wave amplitudes and

$A = 0.05$ m again represents a highly nonlinear wave event. In each case, the errors in the total energy remain very small when the evolution of the wavefield is essentially linear. As the nonlinearity increases, both locally within a given sea state and with increasing A, the maximum errors inevitably increase. However, even in the most nonlinear cases, the maximum error in the total energy is always less than 0.01%.

5. MODEL IMPLEMENTATION AND PRELIMINARY RESULTS

5.1. Initial Conditions

To commence simulations using the proposed model, η and Φ must be defined at each of the calculation points across the entire water surface. This task is complicated by two facts. First, the evolution of a wavefield is traditionally observed in time at a fixed spatial location, with the corresponding wave spectrum represented by a distribution in the frequency domain. Second, with the proposed method based on Fourier analysis, the required description in the spatial domain must be periodic (Eq. (8)).

To explain how these difficulties are overcome, we will first consider a unidirectional wavefield. In the first stage of the analysis, the frequency spectrum must be represented by a set of discrete amplitude components in the wavenumber domain, where the number of components should be an integer power of 2 to maximize the efficiency of the FFTs. Details of the procedure to define these wavenumber components vary depending on whether the model is applied to laboratory data, for which the input is defined by a time-series sent to the wave paddle, or full-scale field data in which $S_{\eta\eta}$ defines a continuous distribution of energy in the frequency domain. Nevertheless, both procedures are based on the assumption that the information in the frequency (or time) domain defines the underlying linear or freely propagating waves.

With a set of discrete wavenumber components identified, the corresponding values of η and Φ may be based on a simple analytical theory, either linear or second order. Since the present paper is primarily concerned with the description of highly nonlinear transient waves, arising due to the focusing of wave components, a linear or second-order solution provides an appropriate description of the initial conditions provided they are specified well in advance of the focal time. At this point, the wave energy is widely dispersed across the computational domain, and the local nonlinear interactions are thereby reduced to a minimum. In an earlier study, Johannessen [24] showed that provided the second-order correction [4] to the maximum initial water surface elevation is no greater than 2%, a linearly predicted η and Φ are sufficient. In the present, study, an alternative and more rigorous condition is applied. Repeated tests suggest that provided the second-order corrections are no greater than 3%, the second-order solution can be used to generate improved initial conditions.

To define the initial conditions appropriate to a directionally spread wavefield, a similar process to that defined above is applied. However, in generating a unidirectional wavefield propagating at, say, 20° to the x-axis, as shown on Fig. 3, it is clear that in a 2-D wavenumber spectrum involving two horizontal directions (k, l), there is no sequential line of components that travel at exactly this angle. Indeed, this condition only exists for waves propagating at 0°, 45°, and 90°. To overcome this difficulty, the appropriate wave energy must be located in wavenumber components which are positioned immediately alongside the desired direction. In Fig. 3 the intersections between the 20° line and the underlying 2-D wavenumber grid

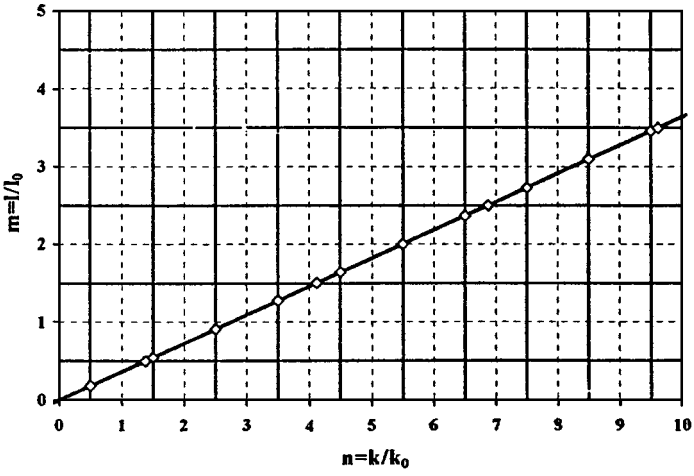

FIG. 3. Diagram of a discrete 3-D spectral grid. The thick line indicates the ideal location for all energy, in order to define a wave travelling at 20° to the x-axis. The solid grid lines represent the edges of discrete cells, the centers of which are defined by the intersection of the dashed lines. These centers represent the position, in wavenumber space, at which the model can ascribe discrete energy.

are noted by the open symbols. The distance between successive symbols indicates the contribution of wave amplitude (or wave energy) from the unidirectional spectrum to be placed within the corresponding grid.

For example, if the distance from the origin in wavenumber space is defined by $K = \sqrt{k^2 + l^2}$, the contribution to the wave motion that should be located in the grid spanned by two successive points K_a and K_b is given by

$$a_{lk}(K_a, K_b) = \int_{K_a}^{K_b} \hat{a}(K, \theta)\, dK, \tag{27}$$

where the unidirectional amplitude spectrum $\hat{a}(K, \theta)$, orientated at some angle θ to the x-axis, is taken to be continuous. In practice, it is usual to assume that $\hat{a}(K, \theta) = \alpha(\theta)\, \hat{a}(K)$, where $\alpha(\theta)$ is the proportion of the total amplitude that propagates at any given angle. There are two commonly applied formulae used to describe the directional distribution. The first, due to Mitsuyasu [25], describes the energy distribution as proportional to $\cos^{2s}(\theta/2)$, giving an amplitude distribution of

$$\alpha(\theta) = \zeta \cos^s\left(\frac{\theta}{2}\right). \tag{28a}$$

Alternatively, the second applies a wrapped normal distribution

$$\alpha(\theta) = \frac{\zeta}{\sigma_\theta} \exp\left(-\frac{\theta^2}{2\sigma_\theta^2}\right), \tag{28b}$$

where the angle θ is measured from the mean wave direction (which in the present cases is aligned with the x-axis), ζ is a normalizing coefficient, s is the Mitsuyasu's spreading parameter, and σ_θ is the standard deviation of the normal distribution.

To describe a directionally spread wavefield, the above process is merely repeated for a large number of individual directions, and the distributed amplitudes are linearly summed.

It is, however, important to note that the angular resolution improves with distance from the origin. Accordingly, when modeling a directionally spread sea, the wavenumber domain (nk_0, ml_0) should be chosen so that the dominant wave energy component, corresponding to the spectral peak, is positioned as far as is possible from the origin ($n = m = 0$). Having again identified a discrete set of wavenumber components, the corresponding values of η and Φ can be calculated using linear or second-order theory, where the latter should be based on Longuet-Higgins [26] for infinite depth or Sharma and Dean [5] for finite depths.

5.2. Model Parameters

Having defined the initial conditions, the model parameters N_x, N_y, k_0, l_0, and Δt need to be chosen so that the desired wavefield can be accurately represented, while remaining within the practical bounds of current computing capabilities. N_x and N_y define the size of the numerical domain in each of the principal coordinate directions. These values must be sufficiently large to capture specific features of the water surface profile, particularly its steepness, but should not be excessively large since this encourages the growth of high-frequency numerical errors. Typical calculations have been based upon domains of size $N = 256 \times 256$, although some cases of 512×512 have also been undertaken.

The fundamental wavenumbers k_0 and l_0 must be sufficiently small to ensure that there are enough wavenumber components in the most energetic parts of the spectrum. In the present study, this was achieved by setting the (weighted) mean position of a spectrum, in each of the principal coordinate directions, to be approximately 1/10th of the size of the domain:

$$\frac{\sum_{l=0}^{\infty}\sum_{k=0}^{\infty} a_{kl}^2 k}{\sum_{l=0}^{\infty}\sum_{k=0}^{\infty} a_{kl}^2} \approx \frac{1}{20} k_0 N_x \quad \text{and} \quad \frac{\sum_{l=0}^{\infty}\sum_{k=0}^{\infty} a_{kl}^2 l}{\sum_{l=0}^{\infty}\sum_{k=0}^{\infty} a_{kl}^2} \approx \frac{1}{20} l_0 N_y. \tag{29}$$

Finally, the time step Δt used in Eqs. (24a) and (24b), was typically chosen so that $\Delta t \leq T_p/200$, where T_p is the time period corresponding to the peak spectral frequency. This choice was simply based upon the experience gained from running a large number of trial simulations, with varying time steps, in which the accuracy and stability of the solution was examined.

5.3. Preliminary Results

To gauge the success of the proposed model, a number of preliminary tests were undertaken. The first concerns a series of unidirectional regular waves in deep water with a wave period of $T = 1.4$ s and a wave steepness of $Hk/2 = 0.3$. This represents approximately 70% of the conventional breaking limit, $Hk/2 = 0.44$, for unidirectional regular waves. The initial conditions used to generate these waves were based upon an analytical fifth-order Stokes expansion [19]. Calculations were undertaken in the fully 3-D computational domain of infinite depth, with unidirectional waves propagating at 0°, 20°, and 45° to the x-axis. Comparisons between these results and the analytical solution for $\eta(t)$ are provided on Fig. 4a. These results confirm that the proposed solution is capable of accurately simulating nonlinear waves propagating at any angle across the computational domain.

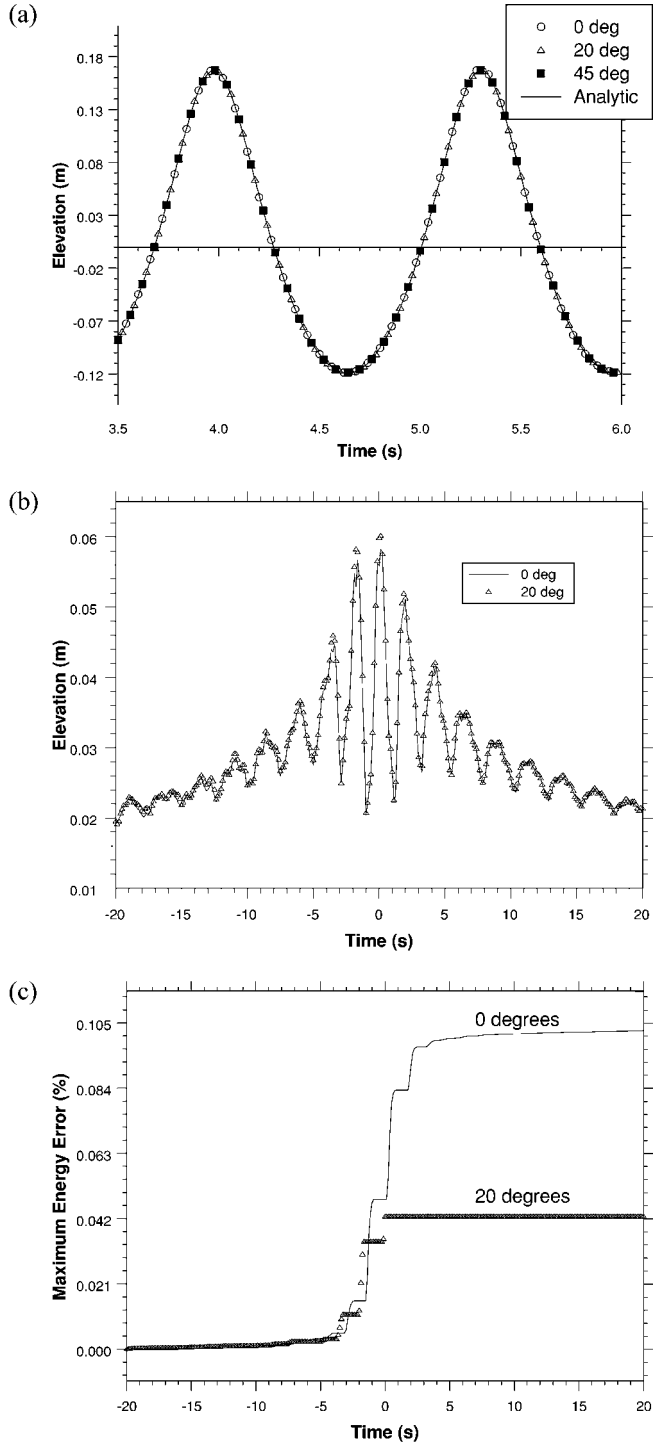

FIG. 4. Preliminary test results. (a) Comparison between the simulation of steady Stokes waves ($ak = 0.3$) at different angles across a numerical domain. $N = 128 \times 128$. (b) A comparison of the maximum surface elevation for two unidirectional waves travelling at 0° and 20° across an uneven spectral mesh, i.e., $\lambda_x = 30$ m, $\lambda_y = 50$ m, $N = 256 \times 256$. (c) The numerical errors arising during the simulation of unidirectional waves travelling at 0° and 20°. The 0° run corresponds to a 2-D simulation with $\lambda = 28.2$ m, which is equivalent to the fundamental wavelengths of $\lambda_x = \lambda_y = 30$ m for the 20° case that was simulated with the 3-D model. $N = 256 \times 256$.

Figures 4b and 4c concern a second series of tests in which a laboratory-scale sea state, involving a unidirectional broadbanded frequency spectrum, was focused to produce a highly nonlinear, near-breaking, wave event at $t = 0$. Figure 4b contrasts the time-variation in the maximum water surface elevation anywhere within the computational domain. Two cases are considered: the first propagating at 0° and the second at 20°. To further complicate these comparisons, the underlying spectral mesh is asymmetric with $\lambda_x = 30$ m and $\lambda_y = 50$ m. Nevertheless, the computed results are again in very good agreement, confirming that the evolution of highly nonlinear transient waves can be successfully modeled and the results shown to be independent of the direction of propagation. Figure 4c concerns the same wave cases and describes the maximum percentage error in the total energy (Eq. (26)). These results appear to suggest that a directional simulation may be more accurate than the equivalent unidirectional case. This probably arises due to three competing effects. First, there is a loss of accuracy due to a reduction of the fundamental wavelength in the principal wave direction (for $\lambda_x = \lambda_y = 30$ m, the effective fundamental wavelength at 20° is 28.1 m). Second, there is a net gain in the mathematical precision achieved by spreading the surface across an additional dimension. This effect is associated with a reduction in the magnitude of the principal horizontal derivatives (corresponding to the x and y directions), which can therefore be more accurately manipulated. Thirdly, there is also a loss of numerical accuracy from further rounding errors associated with the additional dimension. Figure 4c highlights the importance of these competing effects and suggests that the maximum error in the total energy for a wave propagating at 20° is less than half the value for an identical wave propagating along the x-axis (0°). This suggests directionally spread wavefields are slightly easier to model than unidirectional waves, albeit requiring considerably more computer resources. Further details concerning all aspects of the numerical model, its implementation, and additional preliminary tests are given by Bateman [27].

6. DISCUSSION OF RESULTS

6.1. Comparison with Laboratory Data

Recent laboratory data provided by [3] allows further rigorous assessment of the proposed model. This experimental study provides the first detailed measurements of a large number of focused wave groups spread in both frequency and direction. In particular, it includes several cases that were observed to be on the limit of wave breaking. Two underlying frequency spectra were considered: Case B, classified as broadbanded ($0.6 \leq T \leq 1.4$ s); and Case D, classified as narrow-banded ($0.8 \leq T \leq 1.2$ s). In each of these cases, the sea state comprises a large number of wave components, equally spaced within the given period range and of equal amplitude, simultaneously generated at the wave paddles. The direction of propagation and the relative phasing of the wave components were adjusted so that wave focusing produces a large isolated wave crest at one point in space and time. Six directional distributions were considered corresponding to $s = \infty$ (or unidirectional), $s = 150$, $s = 45$, $s = 25$, $s = 10$, and $s = 4$ in Eq. (28a).

For each combination of wave spectrum $S_{\eta\eta}(\omega)$ and directional spread s, a range of input amplitudes (A) were considered, where A defines the linear sum of the component wave amplitudes $A = \sum_{n=1}^{N} a_n$, where a_n is the amplitude of the nth wave component. Given the nature of the focusing event, A also corresponds to the linearly predicted crest elevation at the focal position. To distinguish between the various test cases, the notation

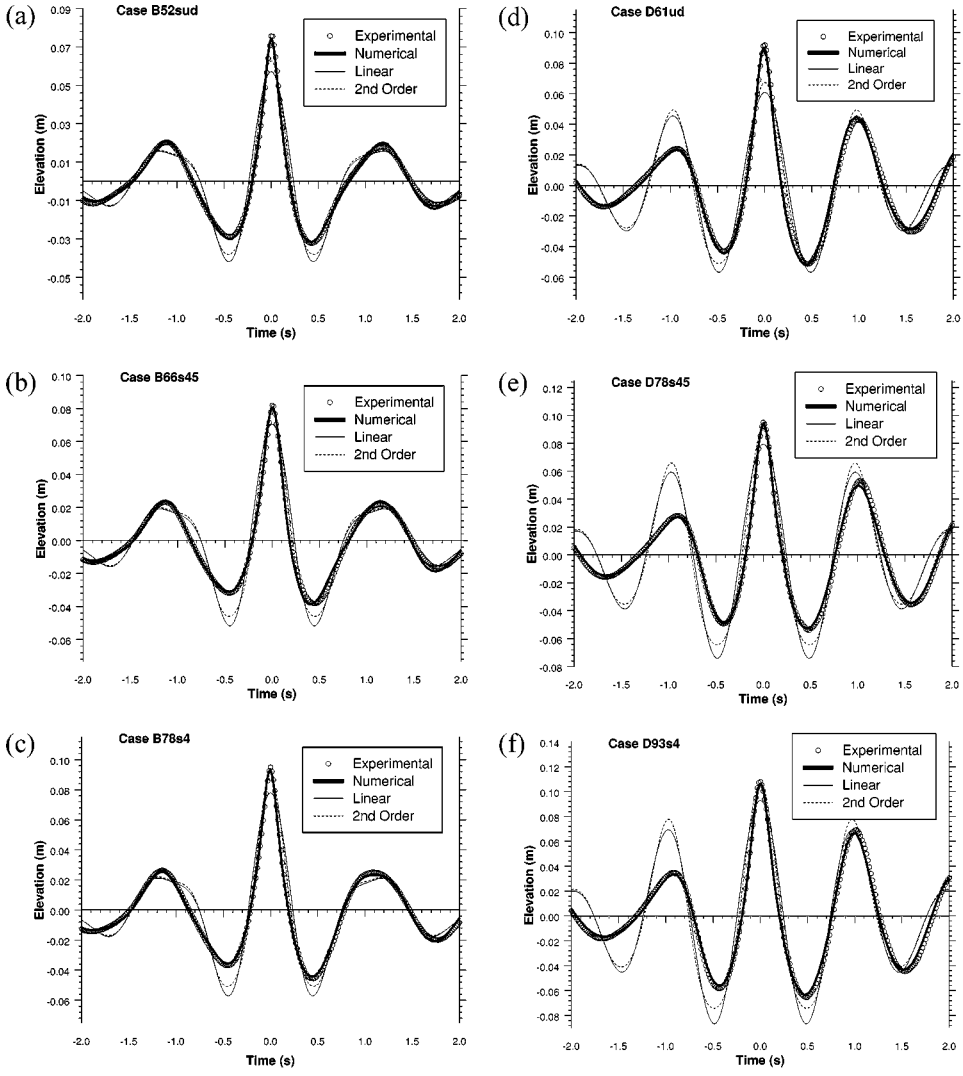

FIG. 5. Temporal records of the water surface elevation, $\eta(t)$, at the focal position ($x = 0$) for unidirectional and directionally spread waves. (a), (b), and (c) correspond to broadbanded frequency spectra, Case B, and (d), (e), and (f) the narrow-banded frequency spectra, Case D.

adopted by Johannessen and Swan [3] will be applied herein. Accordingly, specific test cases are referred to by their input frequency spectrum, their linear amplitude sum, and their directional spread. For example, Case B66s45 corresponds to the broadbanded frequency spectrum (Case B) with an input amplitude of $A = 66$ mm and a directional spread of $s = 45$.

Figures 5a–5f concern the time-history of the water surface elevation $\eta(t)$ recorded at (or very close to) the focal position for six highly nonlinear wave events. In each case, the input amplitude is within 4% of the limiting value at which wave breaking is first observed. The six cases concern both broadbanded and narrow-banded frequency spectra and involve a range of directional spreads from $s = \infty$ (or unidirectional waves denoted by "ud"), directionally spread but relatively long-crested waves corresponding to $s = 45$, and very

short-crested waves with a large directional spread corresponding to $s = 4$. In each case, the numerical model is shown to be in good agreement with the laboratory data. This is particularly true prior to, and in the immediate vicinity of, the focal event ($t = 0$). However, at larger times after focusing $t > 1.0$ s, there are small differences between the observed and numerically predicted results. These are perhaps more evident in the narrow-banded spectra (Figs. 5d–5f). This is consistent with the effects of wave reflection from the downstream boundary of the wave basin, a full discussion of which is given by Johannessen and Swan [3].

Indeed, it is important to note that while the experimental procedure adopted by [3] was specifically arranged to minimize the effects of reflection on the extreme wave event, wave reflections present a significant problem in any 3-D wave basin. Nevertheless, the description provided by the numerical model is very good and significantly better than either the linear or the second-order solutions also presented on Figs. 5a–5f. Indeed, it is interesting to note that while the second-order solution provides an improved fit (relative to linear theory) of the extreme wave crest, particularly as the directionality increases, it provides a poor description of the adjacent wave troughs. This arises because the second-order model cannot incorporate the local energy shifts highlighted by [3] and shown to be very significant in the description of highly nonlinear wave events. The present numerical scheme has no such limitations.

Figures 6a and 6b concern an alternative spatial representation of the water surface elevation, $\eta(x)$, at the instant of wave focusing. Two examples are provided corresponding to B55ud and D93s4. The latter case has both the largest input amplitude sum and the largest directional spread and is in some respects the most difficult case to model. However, in both this case and the unidirectional case, the numerical model is again in very good agreement with the laborator data.

Given the inherent difficulty of obtaining laboratory data in the spatial domain, $\eta(x)$, Figs. 7a–7d and 8a–8d concern Cases B66s45 and D78s45, respectively, and provide time-histories of the water surface elevation at four spatial locations on either side of the focal position ($x = 0$). These results confirm that the numerical model is not only able to model the characteristics of an extreme wave event, but also able to model the evolution of a highly nonlinear and directionally spread wavefield in both space and time.

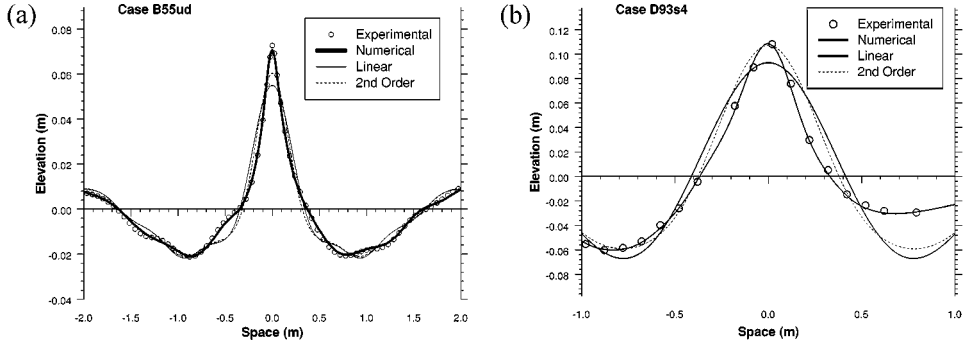

FIG. 6. Spatial records of the water surface elevation, $\eta(x)$, at the focal time ($t = 0$). (a) Case B55ud. (b) Case D93s4.

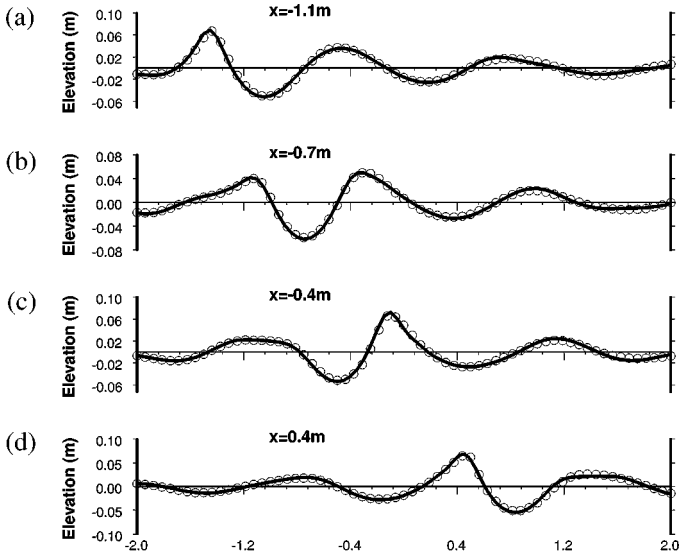

FIG. 7. Temporal profiles of $\eta(t)$ at spatial positions either side of the nonlinear focal event. Case B66s45. (a) $x = -1.1$ m, (b) $x = -0.7$ m, (c) $x = -0.4$ m, and (d) $x = 0.4$ m.

6.2. Simulations of Extreme Ocean Waves

The results presented in Sections 5.3 and 6.1 suggest that the proposed model is both accurate and stable. More significantly, its computational efficiency is such that it provides the first realistic opportunity to model, in a fully nonlinear sense, the characteristics of extreme ocean waves involving a spread of energy in both frequency and direction. Field measurements confirm that the empirical JONSWAP spectrum is appropriate to the description of

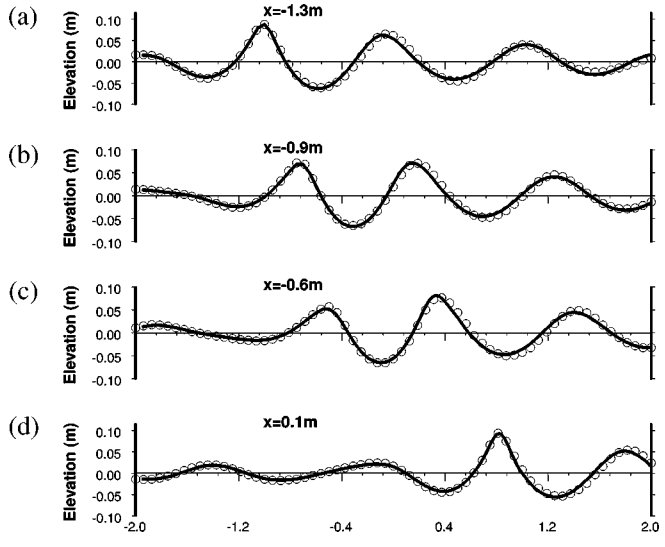

FIG. 8. Temporal profiles of $\eta(t)$ at spatial positions either side of the nonlinear focal event. Case D78s45. (a) $x = -1.3$ m, (b) $x = -0.9$ m, (c) $x = -0.6$ m, (d) $x = 0.1$ m.

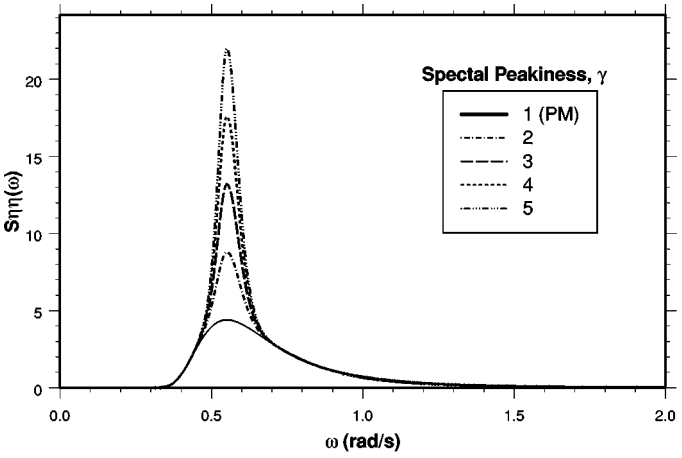

FIG. 9. JONSWAP spectra for $\omega_p = 0.551$ rad/s with variations to the peak enhancement factor, γ. (Note: when $\gamma = 1$, a JONSWAP spectrum corresponds to a Pierson-Moskowitz or PM spectrum).

real ocean spectra in fetch-limited seas,

$$S_{\eta\eta}(\omega) = \frac{\alpha g^2}{\omega^5} \exp\left(-\beta \frac{\omega_p^4}{\omega^4}\right) \gamma^{\exp\left[-\frac{(\omega-\omega_p)^2}{2\omega_p^2\sigma^2}\right]} \quad \sigma = 0.07, \omega \le \omega_p \quad \sigma = 0.09, \omega > \omega_p, \tag{30}$$

where typically $\alpha = 0.0081$, $\beta = 1.25$, ω_p is the peak spectral frequency, and γ is the peak enhancement factor usually chosen to be between 2.8 and 3.0 for severe storm conditions.

A graphical representation of this distribution is given in Fig. 9. An important factor to note is that although the dominant wave energy is relatively narrow banded, the high-frequency tail introduces a significant range of time scales (approximately 1:3 in terms of ω_p). Furthermore, simple linear arguments define the deep water dispersion equation as $\omega^2 = gk$, suggesting that the range of significant length scales is at least of order 1:10. To incorporate this range, and at the same time to allow the model sufficient opportunity to describe the local energy shifts in the vicinity of an extreme event (involving both high and low frequencies), the resolution in the directional wavenumber domain (k, l) must be high. This, in turn, implies a large number of surface points within the computational domain, and explains the overriding need for computational efficiency.

Early work by Lindgren [28], together with more recent contributions from Boccotti [29], Phillips *et al.* [30], and Tromans *et al.* [31], has shown that the most probable or average shape of a large wave event (provided $A/\sigma_\eta > 2$ where σ_η is the standard deviation of the surface elevation, $\eta(t)$) is related to the autocovariance function of the underlying spectrum. Although the arguments underlying this result are fundamentally linear, assuming that all the wave components are freely propagating, it can be manipulated to yield the initial conditions appropriate to the proposed model. The steps associated with this task are as follows:

(a) The NewWave model [31] is applied to define the linearly predicted shape of an extreme wave (specified in terms of $A = \eta_{\max}$) with the desired underlying frequency spectrum

($S_{\eta\eta}(\omega)$ in Eq. (30)). In the time domain this gives the expected shape of a large wave event as

$$\eta(t) = \eta_{\max} \frac{\int_0^\infty S_{\eta\eta}(\omega) \cos(\omega t)\, d\omega}{\int_0^\infty S_{\eta\eta}(\omega)\, d\omega}. \tag{31}$$

For this wave event the amplitude spectrum of discrete wavenumber components is obtained from

$$a(k) = \eta_{\max} \frac{S_{\eta\eta}(\omega(k))}{\int_0^\infty S_{\eta\eta}(\omega)\, d\omega} \Delta\omega, \tag{32}$$

where $w(k) = \sqrt{gk \tanh(kh)}$ and $\Delta\omega$ is the frequency interval corresponding to the discretization of the wavenumber spectrum.

(b) These discrete wave components are back calculated (linearly) to an initial time, well before the extreme or focal event, at which the wave energy is widely dispersed (Section 5.1). Such calculations must include the effects of directionality modeled using either Eqs. (28a) or (28b).

(c) A simple linear or second-order analytical solution is used to generate the corresponding initial values for $\eta(x, y)$ and $\Phi(x, y)$ appropriate to the numerical model.

(d) Using these initial conditions the wavefield is time marched, in a fully nonlinear sense, up to and beyond the occurrence of an extreme focused event. Due to the nonlinear interactions, this extreme event will occur at neither the linear focal time nor the linear focal position. Nevertheless, comparisons between the nonlinear extreme event and the original linear predictions (Eq. (31)) highlights the importance of nonlinearity when defining an extreme ocean wave.

The results of this process are given in Figs. 10a–10h. These calculations correspond to a JONSWAP spectrum with $\omega_p = 0.46 s^{-1}$ and $\gamma = 1.7$, a directional distribution of $s = 7$ (or $\sigma_\theta = 30^\circ$ in Eq. (28b)) and a linear input amplitude sum of $A = 16.3$ m. This case corresponds to a typical design wave for the northern North Sea with a return period of 10,000 years. Figures 10a–10h provide a sequence of 3-D spatial plots defining the water surface elevation, $\eta(x, y)$, at discrete times in the vicinity of an extreme or focal event occurring at $t = 1.6$ s. The sequence commences at $t = -100$ s (Fig. 10a) and continues past the focal point to $t = +30$ s in Fig. 10h. The initial conditions appropriate to this case were specified using linear theory at $t = -100$ s. The calculations incorporated 256×256 wavenumber components with $\lambda_x = \lambda_y = 4000$ m. To provide a good visual description of the evolving wavefield each part of Fig. 10 concerns a small central region of the computational domain, covering 25% of the total area.

The characteristics of the extreme wave occurring at $t = 1.6$ s on Fig. 10d is further investigated in Fig. 11. This provides a spatial description of the water surface elevation in the mean wave direction, $\eta(x)$, and contrasts the fully nonlinear calculations with a linear solution based upon the summation of the freely propagating wave components implemented within the initial conditions. As a large wave evolves, the nonlinear wave–wave interactions cause a "downstream-shifting" of both the focal-position and the focal-time. In the present example, the nonlinear wave focused at $x = 80$ m. However, this effect has been removed from the present comparisons in order to highlight the significant nonlinear changes in the

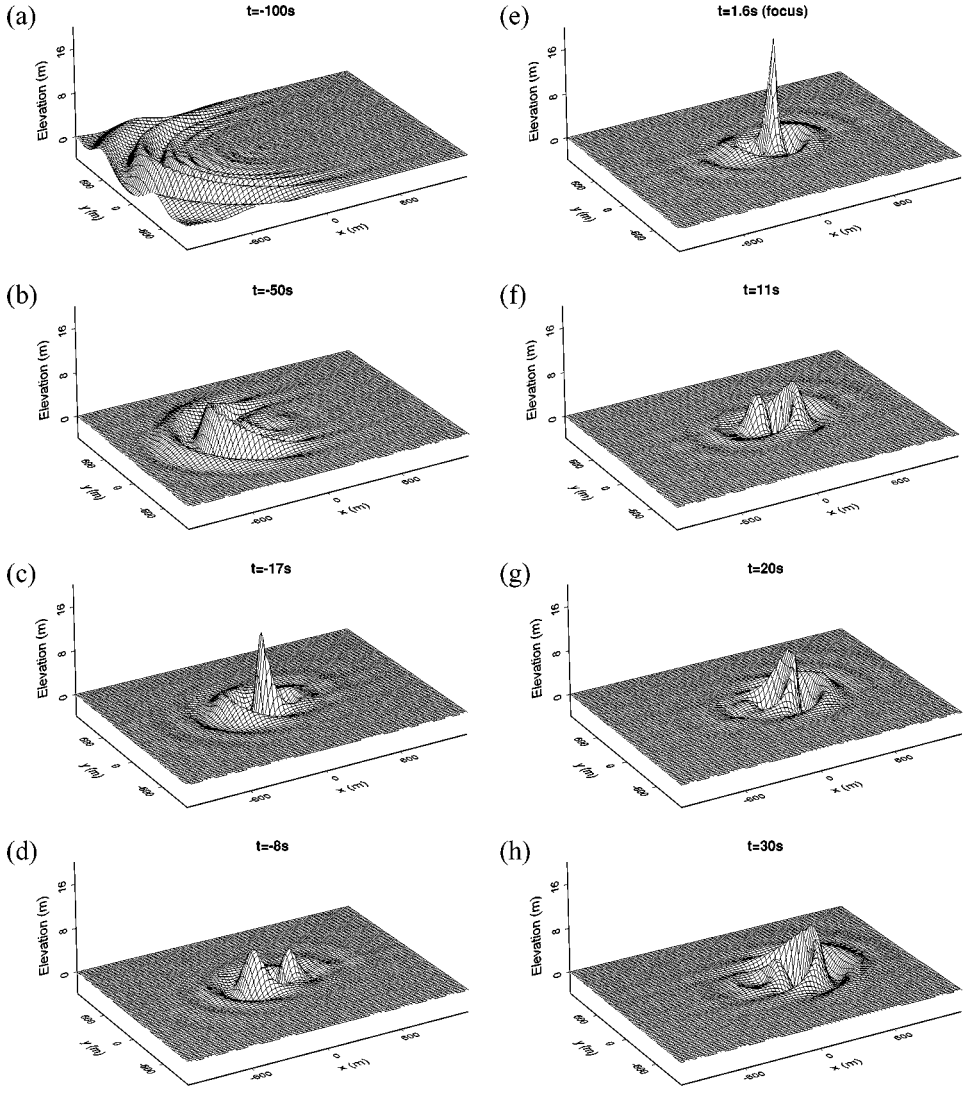

FIG. 10. Evolution of a short-crested, directionally spread, $s = 7$, steep wave group. $T_p = 13.5$ s, $h = \infty$, $\gamma = 1.7$.

profile of the extreme wave. In particular, the largest wave crest is shown to be higher and narrower than the linear predictions due to the local nonlinear energy transfers within the wavenumber domain.

The fundamental importance of the directionality of a sea state is demonstrated by comparison with the fully nonlinear, unidirectional wave record indicated by the dashed line on Fig. 11. This record is based upon an identical (normalized) wave spectrum, $S_{\eta\eta}(\omega)$, and represents the largest nonbreaking wave that can be generated in a unidirectional sea ($s = \infty$). The difference between this and the fully nonlinear directionally spread wave record is consistent with the laboratory findings of [3]. In particular, it confirms their hypothesis that an increase in the directionality of a wavefield allows larger waves to evolve prior to the onset of wave breaking.

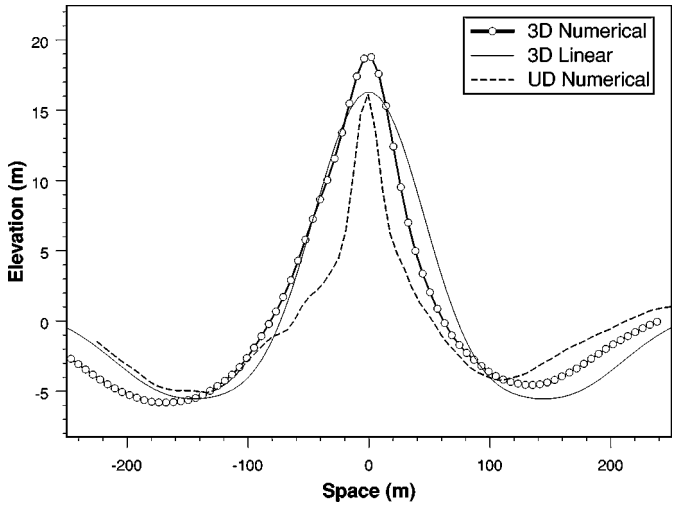

FIG. 11. Spatial records of the water surface elevation, $\eta(x)$, at the focal time ($t = 0$) for the near-breaking unidirectional ($s = \infty$) and directional ($s = 7$) waves. $\gamma = 1.7$, $T_p = 13.5$ s, $h = \infty$.

7. CONCLUDING REMARKS

This paper has considered the description of surface water waves, particularly the evolution of extreme waves due to the focusing of wave components involving a significant spread of energy in both frequency and direction. Such waves are highly nonlinear, evolving in both space and time. To model such waves a new, fully nonlinear, spectral wave model has been proposed. This is based upon a form of the Dirichlet–Neumann operator similar to the G-operator employed in the unidirectional wave model proposed by Craig and Sulem [13]. Using this approach, an initial spatial representation of the water surface, $\eta(x, y)$, and the velocity potential at this surface, $\phi(x, y, \eta) = \Phi(x, y)$ can be time marched to define the evolution of a wavefield. Furthermore, by representing both η and Φ as Fourier series, the necessary spatial derivatives can be calculated rapidly using fast Fourier transforms. The overriding advantage of this technique lies in its computational efficiency and hence its ability to model the large range of length scales, in two coordinate directions (x, y), associated with realistic ocean waves. Indeed, the present model provides the only solution capable of modeling, in a fully nonlinear sense, the evolution of extreme 3-D ocean waves.

The proposed model has been validated using existing regular wave theories and, perhaps more importantly, by comparison with recent laboratory data describing extreme, near-breaking waves in a directionally spread sea [3]. This data set is significant in that it provides the first quantitative assessment of the importance of directionality in determining the characteristics of extreme waves. In particular, it shows that for a constant input amplitude sum (or constant energy level) an increase in the directionality leads to reduced nonlinearity and hence lower crest elevations. Conversely, if the energy level is increased until the onset of wave breaking, an increase in directionality leads to larger limiting crest elevations. The present model is able to reproduce accurately these effects at a laboratory scale. More significantly, it has also demonstrated (for the first time) that similar effects may occur in the open ocean involving realistic frequency spectra and directional spreads.

The success of the present model is important in two respects. First, there are significant limitations as to what can be investigated in a laboratory-scale wave basin. For example, Johannessen and Swan [3] identify some significant and unexpected nonlinear wave–wave interactions in the vicinity of an extreme event and provide some evidence that the associated wave components are freely propagating. However, due to the inherent difficulty of obtaining accurate, well-resolved spatial data, $\eta(x, y)$, the precise nature of these wave components could not be resolved. The present model provides an ideal vehicle to investigate this point. Secondly, from a more practical perspective, the description of extreme ocean waves is fundamental to the safe and economic design of both fixed and floating structures. Recent events, involving the impact of wave crests on the underside of fixed structures, the green-water inundation of moored structures, and the continued loss of shipping (involving both large and small vessels) suggests that there are aspects of the ocean wave environment that are not well modeled. Indeed, there is much on-going discussion of so-called "freak" waves, or those which are larger or occur more often than is statistically predicted. The present model provides an important tool with which to investigate these practically important events and to identify if there are new physical processes associated with the occurrence of extreme ocean waves.

REFERENCES

1. P. Jonathan and P. H. Taylor, Irregular nonlinear waves in a spread sea, *ASME Trans. J. Offshore Mech. Arctic Eng.* **119**, 37 (1996).
2. T. E. Baldock, C. Swan, and P. H. Taylor, A laboratory study of non-linear surface waves on water, *Phil. Trans. Roy. Soc. London. Ser. A* **354**, 649 (1996).
3. T. B. Johannessen and C. Swan, A laboratory study of the focusing of transient and directionally spread surface water waves, *Proc. Roy. Soc., Ser. A* **457**, 1 (2001).
4. M. S. Longuet-Higgins and R. W. Stewart, Changes in the form of short gravity waves on long waves and tidal currents, *J. Fluid Mech.* **8**, 565 (1960).
5. J. N. Sharma and R. G. Dean, Second-order directional seas and associated wave forces, *Soc. Pet. Eng. J.* **4**, 129 (1981).
6. T. B. Benjamin and J. E. Feir, The disintergration of wave trains on deep water. Part 1: Theor, *J. Fluid Mech.* **27**, 417 (1967).
7. E. Lo and C. C. Mei, A numerical study of water-wave modulation based on a higher order Schrdinger equation, *J. Fluid Mech.* **150**, 395 (1985).
8. M. S. Longuet-Higgins and E. D. Cokelet, The deformation of steep surface waves on water. A numerical method of computation, *Proc. Roy. Soc., Ser A* **350**, 1 (1976).
9. T. B. Johannessen and C. Swan, The nonlinear dynamics of focussed wave groups in two and three dimensions, submitted for publication.
10. J. D. Fenton and M. M. Rienecker, A Fourier method for solving nonlinear water-wave problems: application to solitary-wave interactions, *J. Fluid Mech.* **118**, 411 (1982).
11. J. W. Dold and D. H. Peregrine, Steep unsteady waves: an efficient computational scheme, *Proc. 19th Int. Conf. Coastal Eng. ASCE* **1**, 90 (1984).
12. M. Isaacson and K. F. Cheung, Second-order wave diffraction in three dimensions, *J. Waterway, Port, Coastal Ocean Eng., ASCE*, **118** 496 (1992).
13. W. Craig and C. Sulem, Numerical simulation of gravity waves, *J. Comput. Phys.* **108**, 73 (1993).
14. R. R. Coifman and Y. Meyer, Nonlinear harmonic analysis and analytic dependence, *Proc. Symp. Pure Math.* **43**, 71 (1985).
15. W. Craig, U. Schanz, and C. Sulem, The modulation limit of three-dimensional water waves, and the Davey-Stewartson system, *Annales de. 1'IHP: Analyse Nonlineaire* **14**, 615 (1997).

16. D. P. Nicholls, Traveling water waves: Spectral continuation methods with parallel implementation, *J. Comput. Phys.* **143**, 224 (1998).
17. S. Slepian, Some comments on the Fourier Analysis Uncertainty Modeling, *SIAM Rev.* **25**, 379 (1983).
18. E. M. Vijfvinkel, *Focused Wave Groups on Deep and Shallow Water*, M.Sc. thesis. (University of Groningen, The Netherlands, 1996).
19. J. D. Fenton, A fifth order Stokes' theory for steady waves, *J. Waterways, Port, Coastal Eng.* **1**, 216 (1985).
20. M. Frigo and S. G. Johnson, The Fastest Fourier Transform in the West, MIT-LCS-TR-728, available at http://theory.lcs.mit.edu/fftw/.
21. W. H. Press, S. A. Teukolsky, W. T. Vetterling, and B. P. Flannery, *Numerical Recipes in C—The Art of Scientific Computing*, 2nd ed. (Cambridge Univ. Press, Cambridge, UK, 1994).
22. D. G. Dommermuth and D. K. P. Yue, A high-order spectral method for the study of nonlinear gravity waves, *J. Fluid Mech.* **184**, 267 (1987).
23. T. B. Benjamin and P. J. Olver, Hamiltonian structure, symmetries and conservation laws of water waves, *J. Fluid Mech.* **125**, 137 (1982).
24. T. B. Johannessen, The Effect of Directionality on the Nonlinear Behaviour of Extreme Transient Ocean Waves, Ph.D. thesis (Imperial College, University of London, 1997).
25. H. Mitsuyasu, Observation of directional spectrum of ocean waves using a cloverleaf buoy, *J. Phys. Oceanogr.* **16**, 459 (1975).
26. M. S. Longuet-Higgins, The effect of non-linearities on statistical distributions in the theory of sea waves, *J. Fluid Mech.* **17**, 459 (1963).
27. W. J. D. Bateman, A Numerical Investigation of Three Dimensional Extreme Water Waves, Ph.D. thesis (Imperial College, University of London, 2000).
28. G. Lindgren, Some properties of a normal process near a local maximum, *Ann. Math. Stat.* **41**, 1870 (1970).
29. P. Boccotti, Some new results on statistical properties of wind waves, *Appl. Ocean Res* **5**, 134 (1983).
30. O. M. Phillips, D. Gu, and E. J. Walsh, Expected structure of extreme waves in a Gaussian sea. Part 1: Theory and SWADE buoy measurements, *J. Phys. Ocean. ogr.* **23**, 992 (1993).
31. P. S. Tromans, A. R. Anaturk, and P. Hagemeijer, A new model for the kinematics of large ocean waves, *Proc. First Intern. Confer. on Offshore and Polar Engineering, Edinburgh, United Kingdom* (1991), Vol. 3, p. 64.